

Submitted to The Astrophysical Journal, 8 September 1998

The Impact of Atmospheric Fluctuations on Degree-scale Imaging of the Cosmic Microwave Background

Oliver P. Lay

Radio Astronomy Laboratory, University of California, Berkeley, CA 94720

and

Nils W. Halverson¹

Dept. of Astronomy and Astrophysics, University of Chicago, 5640 S. Ellis Avenue, Chicago, IL 60637

ABSTRACT

There is currently an active effort to map the spatial variations in the intensity of the cosmic microwave background (CMB), with different experiments utilizing chopped beam, swept beam, and interferometric approaches to minimize systematic errors. Fluctuations in the brightness of the Earth's atmosphere originating from water vapor are an important source of noise for ground-based instruments. This paper presents a model for the fluctuations and derives simple expressions to predict the contribution of the atmosphere to experimental measurements. Data from the South Pole and from the Atacama Desert in Chile, two of the driest places on Earth, are used to assess the level of fluctuations at each site.

The model consists of a layer of turbulence in which the fluctuations follow a modified Kolmogorov power law, with both three- and two-dimensional regimes. The isotropic, three-dimensional case, which applies on small scales, is dominant in most applications. The analysis treats the instruments as window functions that act on the power spectrum of the fluctuations, resulting in a simple pictorial approach analogous to the instrumental window functions that are applied to theoretical models of the CMB angular power spectrum.

The South Pole data are from the Python V experiment, and are used to estimate the level of atmospheric fluctuations over 2 months of the summer. The distribution is bimodal, with long periods of very stable conditions ($\Delta T_{\text{rms}} < 1$ mK in a 6° strip) broken by occasional periods of much stronger fluctuations ($\Delta T_{\text{rms}} > 10$ mK), which appear to be associated with clouds. These periods are correlated with a change in wind direction that brings moist air from West Antarctica.

¹Dept. of Applied Physics, California Institute of Technology, Pasadena, CA 91125

The Atacama Desert in Chile is the proposed location of the Millimeter Array. A site testing interferometer measures fluctuations in the refractive index of the atmosphere, which are also due to water vapor. These data are converted into the equivalent brightness temperature fluctuations; the results suggest that the fluctuations are higher for the Chile site than at the South Pole, although there is a strong dependence on the altitude of the turbulent layer, which is not well constrained. An example calculation for an interferometer is made.

Subject headings: atmospheric effects — instrumentation: interferometers — methods: analytical — cosmic microwave background

1. Introduction

There is currently an active effort to measure the level of anisotropy present in the cosmic microwave background (CMB) from arcminute to degree angular scales. The brightness temperature of the fluctuations are of order 10^{-5} K, requiring carefully designed experiments. Contamination from point sources and galactic dust emission is minimized by choosing an observing frequency of between 20 and 300 GHz (1.5 cm to 1 mm), depending on the angular scale being investigated (Tegmark & Efstathiou 1996). Differential measurements are employed to minimize systematic errors: chopped beam instruments measure the difference in emission between two or more directions on the sky, swept beam instruments sweep a beam rapidly backwards and forwards, and interferometers correlate signals from two or more antennas. Some examples of chopped beam experiments are Python I-IV (Dragovan et al. 1994, Ruhl et al. 1995, Platt et al. 1997, Kovac et al. 1998), OVRO RING5M (Leitch et al. 1998), and Tenerife (Davies et al. 1996). Current or recent swept beam experiments include Python V (Coble et al. 1998), Viper (J. Peterson, personal communication), and the Mobile Anisotropy Telescope (L. Page, personal communication). Interferometers currently being built include the Degree Angular Scale Interferometer (DASI), the Cosmic Background Interferometer (CBI), and the Very Small Array (VSA). In addition, the Cosmic Anisotropy Telescope (CAT) has already been operational for several years (Scott et al. 1996). These employ wide bandwidth, low-noise receivers to maximize sensitivity, and should be deployed at sites where the Earth’s atmosphere does not significantly compromise performance.

The atmosphere is also a source of brightness temperature variations, originating primarily from water molecules. Of the the three states that may be present – vapor, liquid and ice – it is water vapor that is most important. Most of it is contained in the troposphere with a scale height of ~ 2 km, and, because the water vapor is close to its condensation point, it is poorly mixed with the ‘dry’ component of the atmosphere (mostly nitrogen and oxygen). This, in combination with turbulence, leads to a clumpy, non-uniform distribution of water vapor in the troposphere. Since the water molecule has a strong dipole moment, rotational transitions couple

strongly to millimeter-wave radiation, and water vapor is the dominant source of atmospheric emission (and therefore opacity) at most millimeter wavelengths. Liquid water, in the form of clouds, is also a source of non-uniform emission, but radiates much less per molecule. Ice is the least efficient radiator, since the molecules are unable to rotate. Fluctuations in temperature caused by turbulent mixing are also a source of brightness temperature variations, although they are generally much less significant than the water vapor contribution at millimeter wavelengths.

It should also be noted that the high refractive index of water vapor causes an excess propagation delay, and a non-uniform distribution of water vapor distorts an incoming wavefront. This sets a ‘seeing’ limit on interferometric observations at millimeter wavelengths, and there is an ongoing effort to correct for this effect. It is this problem, which limits performance at arcsecond spatial resolution and high frequencies, that has driven much of the recent research into the distribution of water vapor (e.g. Armstrong & Sramek 1982; Treuhaft & Lanyi 1987, Wright 1996, Lay 1997).

The wavefront distortions are not significant for the low resolution experiments considered here. The atmospheric emission fluctuations, however, can only be distinguished from fluctuations in the cosmic background by the wind-induced motion of the atmosphere with respect to the background. This paper investigates how well the two can be separated. The next section describes a model of atmospheric fluctuations and the responses of the different types of instrument. Section 3 describes how data from the Python V experiment have been used to characterize the fluctuations at the South Pole, and Section 4 estimates the level of emission fluctuations for the Atacama Desert in Chile using rms path fluctuation data. Section 5 gives an example of how the theory of Section 2 can be combined with the fluctuation data from each site to predict the residual noise level due to the atmosphere.

2. Models

We present a brief analysis of the theory of atmospheric fluctuations and their impact on astronomical observations. Church (1995) presented a rigorous mathematical analysis based on the autocorrelation function of the fluctuations. We adopt a more pictorial approach based on the power spectrum of the fluctuations, using an atmospheric model that differs in a fundamental way from that assumed by Church. Instrumental configurations are characterized by their spatial and temporal filtering properties, and expressions are derived for the atmospheric contribution to the noise for chopped beam, swept beam and interferometric experiments.

2.1. Model of Atmospheric Emission Fluctuations

We adopt the Kolmogorov model of turbulence (Tatarskii 1961). Turbulent energy is injected into the atmosphere on large scales from processes such as convection and wind shear, and then

cascades down through a series of eddies to smaller scales, until it is dissipated by viscous forces on size scales of order 1 mm. If energy is conserved in the cascade then simple dimensionality arguments can be used to show that the power spectrum of the fluctuations in a large 3-dimensional volume is proportional to $q^{-11/3}$, where q is the spatial wavenumber (units: length^{-1}). This holds from the outer scale size L_o on which the energy is injected to the inner scale size L_i on which it is dissipated. Tatarskii showed that this same power law applies to quantities that are passively entrained in the flow of air, such as the mass fraction of water vapor.

Figure 1 shows the geometry used for this analysis. The water vapor fluctuations are present in a layer of thickness Δh at average altitude h_{av} . The x -, y - and z -axes form an orthogonal set with the z -axis parallel to the line of sight of the observations at elevation ϵ . The fluctuations can be projected onto the $x - y$ plane, perpendicular to the line of sight. The power spectral density function (PSD) of the projected fluctuations for observations in the zenith direction is given by

$$P_{\text{atm}}(q_{xy}) = \begin{cases} Aq_{xy}^{-11/3} & L_i \ll |q_{xy}^{-1}| \ll 2\Delta h \\ A'q_{xy}^{-8/3} & 2\Delta h \ll |q_{xy}^{-1}| \ll L_o \end{cases} \quad (1)$$

where $q_{xy} = (q_x^2 + q_y^2)^{1/2}$. The coefficient A , and the related value A' , are a measure of the turbulent intensity. By adopting units of $\text{K}^2 \text{m}^2$ for P_{atm} , the volume under the PSD gives the mean squared brightness temperature of the emission fluctuations, ΔT_{atm}^2 . For example, if only wavenumbers in the range $(q_x \pm \Delta q_x/2, q_y \pm \Delta q_y/2)$ were considered, then $\Delta T_{\text{atm,rms}} = \sqrt{P_{\text{atm}} \Delta q_x \Delta q_y}$. The first case in Eq. 1, applies to physical scales smaller than Δh , where the turbulence is considered to be isotropic in three dimensions. In the second case the turbulence is infinite horizontally but is constrained vertically to lie in a layer of thickness Δh . The increase towards $(0, 0)$ is less rapid than for the 3D case. Beyond the outer scale the PSD should become constant. It is also implicit that the optical depth through the layer is much less than 1.

The derivation of the $-11/3$ power law by Kolmogorov applies in the isotropic three-dimensional case, well within the inner and outer scales, where the turbulence can be considered scale-free. There is extensive experimental evidence to support this. In previous analyses (e.g. Church 1995, Andreani et al. 1990), it was assumed that there were no correlations present in the turbulent layer on scales greater than the thickness Δh , i.e. Δh corresponded to the outer scale size (outer scale sizes of between 1 m and 100 m were used in Church’s calculations). Data from atmospheric phase monitors operating at 12 GHz (Masson 1994; Holdaway 1995, Lay 1997) and radio telescope arrays such as the Very Large Array (Armstrong & Sramek 1982; Carilli & Holdaway 1997) show no evidence for such a low value of L_o ; indeed, correlation is observed over separations in excess of 10 km. While there may be conditions in which the outer scale length is greatly reduced (Coulman & Vernin 1991), the data are generally well described by a $-11/3$ power law on small scales, and a $-8/3$ power law on large scales, with the transition occurring for sizes comparable to the layer thickness as described in Eq. 1. The $-8/3$ power law for the two-dimensional regime can be derived from similar scaling arguments to the 3D case, but cannot be justified rigorously on theoretical grounds, since turbulence is not strictly possible in

a two-dimensional medium – the layer must have some vertical extent – and the model should therefore be regarded as somewhat empirical.

We convert (q_x, q_y) to angular wavenumbers (α_x, α_y) (units: radians⁻¹) by multiplying by h_{av} , an approximation that only holds for $\alpha_{xy} \gg 1$. Therefore

$$P_{\text{atm}}(\alpha_{xy}) = \begin{cases} Ah_{\text{av}}^{5/3} \alpha_{xy}^{-11/3} & h_{\text{av}}/(2\Delta h) \ll \alpha_{xy} \ll \alpha_i \\ A'h_{\text{av}}^{2/3} \alpha_{xy}^{-8/3} & \alpha_o \ll \alpha_{xy} \ll h_{\text{av}}/(2\Delta h). \end{cases} \quad (2)$$

The transition between the three- and two-dimensional regimes is at approximately $h_{\text{av}}/(2\Delta h)$; α_o and α_i correspond to the outer and inner scales of the turbulence, respectively. A factor of h_{av}^2 is included for the correct normalization of the PSD. This distribution of fluctuation power is shown schematically in Fig. 2.

This treatment has assumed that the observations are in the zenith direction. In the 3D regime, the atmospheric fluctuation power is proportional to the path length through the layer which scales as $1/\sin \epsilon$. In addition, the conversion to angular wavenumber requires a factor $h_{\text{av}}/\sin \epsilon$ (this is the distance to the layer along the line of sight) instead of just h_{av} . Therefore, for the 3D regime ($\alpha_i > \alpha_{xy} \gg h_{\text{av}}/(2\Delta h)$)

$$P_{\text{atm}}(\alpha_{xy}) = \left(\frac{A}{\sin \epsilon} \right) \left(\frac{h_{\text{av}}}{\sin \epsilon} \right)^{5/3} \alpha_{xy}^{-11/3} \quad (3)$$

$$= Ah_{\text{av}}^{5/3} (\sin \epsilon)^{-8/3} \alpha_{xy}^{-11/3}. \quad (4)$$

This prescription for atmosphere fluctuations, valid for small angular scales, is used in §2.4. On larger scales, where the 2D regime becomes more important, the situation has a much more complicated dependence on layer thickness and elevation, and a numerical calculation should be performed (e.g. Treuhaft and Lanyi 1987; Lay 1997).

2.2. Spatial Filtering

Different measurement schemes are sensitive to different ranges of angular wavenumbers. If the angular response of an instrument on the sky is given by $R(\theta_x, \theta_y)$ then the corresponding response to wavenumber is the Fourier Transform, $\hat{R}(\alpha_x, \alpha_y)$. The appropriate filter for the power spectrum of sky fluctuations is $|\hat{R}|^2$. Note that it is important to distinguish between the ‘power’ of atmospheric fluctuations (the square of brightness temperature) and the power (the square of electric field) received from different parts of the sky by an instrument. The former is related to the square of the latter. We assume that the emission fluctuations are present in the far-field of the instrument, i.e. $h_{\text{av}} \gg \frac{D^2}{\lambda}$, so that this analysis does not apply to large telescopes and short wavelengths. Both R and $|\hat{R}|^2$ are depicted schematically in Fig. 3 for three cases: a single aperture that chops between two positions separated by an angle of θ_{chop} , a single aperture that sweeps over a range θ_{sweep} , and an interferometer with a fringe spacing of $\theta_{\text{int}} = \lambda/B$, where λ

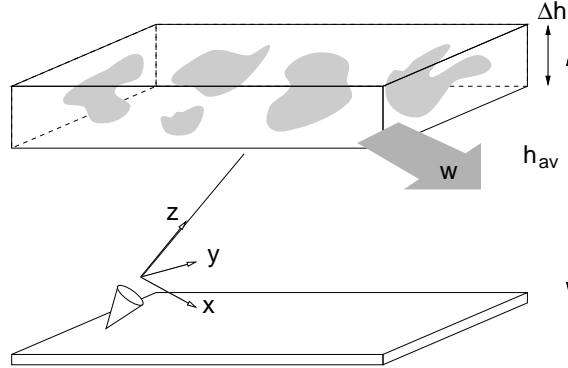


Fig. 1.— Geometry adopted for the analysis. The generic instrument is observing at elevation ϵ through a layer of fluctuations with thickness Δh at average altitude h_{av} that is being blown by wind vector w . The x -, y - and z -axis form an orthogonal set with the z -axis parallel to the line of sight.

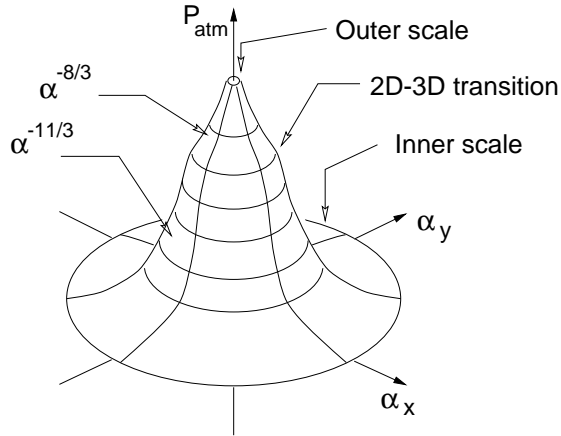


Fig. 2.— Schematic representation of the distribution of atmospheric fluctuation power in the angular wavenumber domain. The combination $\alpha_x = 10$, $\alpha_y = 0$ would correspond to a fluctuation with a periodicity of 0.1 radian (5.7°) in the x -direction. In practice the distribution is distorted within $\alpha_{xy} \sim 1$, since the angular approximation breaks down.

is the observing frequency and B is the length of the baseline perpendicular to the line of sight. In each case θ_b is the Full-Width-to-Half-Maximum (FWHM) size of the power pattern of the beam from the single dish or horn, which we approximate as having a Gaussian profile, and represent schematically as a single circular contour. The Fourier Transform of this single beam is another Gaussian with FWHM of $\alpha_b = 4 \ln 2 / (\pi \theta_b)$, and the corresponding $|\hat{R}|^2$ has a FWHM of $\alpha_b / \sqrt{2} = 0.62 \theta_b^{-1}$. The x -axis is chosen to be parallel to the chop direction, sweep direction and projected baseline vector.

The response $|\hat{R}|^2$ for the chopping instrument is a \sin^2 function with zeroes at $\alpha_x = n \theta_{\text{chop}}^{-1}$, ($n = 0, 1, 2, \dots$). The instrument is insensitive to scales much smaller than the beam size θ_b , corresponding to large values of α .

The swept beam case is slightly more complicated. We assume that the data are sampled at the Nyquist rate to generate $N = 2\theta_{\text{sweep}}/\theta_b$ samples per sweep. An FFT of these data generate N real channels (or alternatively $N/2$ complex channels for $\alpha_x \geq 0$) in the angular wavenumber domain spaced by $\theta_{\text{sweep}}^{-1}$ (dashed lines). This case is different from the single chop, since there are N independently determined quantities, rather than one. In practice, data from the swept ‘slot’ on the sky must to be tapered at the ends to avoid ‘ringing’ effects in the transform. This gives rise to an effective channel width $\Delta\alpha$ that is larger than the channel separation, as indicated by the shaded region in Fig. 3. The beam size again sets an upper limit on the angular wavenumber to which the instrument is sensitive.

The interferometer responds to a range of spatial wavenumbers centered on $\alpha_x = B/\lambda$. It is assumed that a complex correlator is used to measure both the sine and cosine components on the sky; half of the total fluctuation power is present in each component (for the sake of clarity, Fig. 3 shows only the cosine component). Note that the Gaussian profile would imply that the interferometer has a finite response to $(\alpha_x, \alpha_y) = (0, 0)$. In fact there must be zero response and the Gaussian approximation breaks down near the origin, since there is no overlap between the apertures.

2.3. Temporal Filtering

The wind vector \mathbf{w} advects the layer containing the blobs of water vapor in a horizontal direction, so that the distribution of fluctuations projected onto the $x - y$ plane appears to move at speed $\mathbf{w}_{xy} = (w_x, w_y)$, the component of \mathbf{w} parallel to the $x - y$ plane. A fluctuation component characterized by (q_x, q_y) sampled along a line of sight parallel to the z -axis produces a signal that varies in time with frequency $\nu = w_x q_x + w_y q_y$.

Time-averaging the output of an instrument is equivalent to a low pass filter which rejects signals that are varying rapidly. Averaging over t_{av} has an associated frequency power response function $|\hat{T}(\nu)|^2 = \text{sinc}^2(\pi\nu t_{\text{av}})$, which can be approximated by a rectangular function with an equivalent half-width of $(2t_{\text{av}})^{-1}$. This response to ν can be mapped to the (α_x, α_y) plane using the

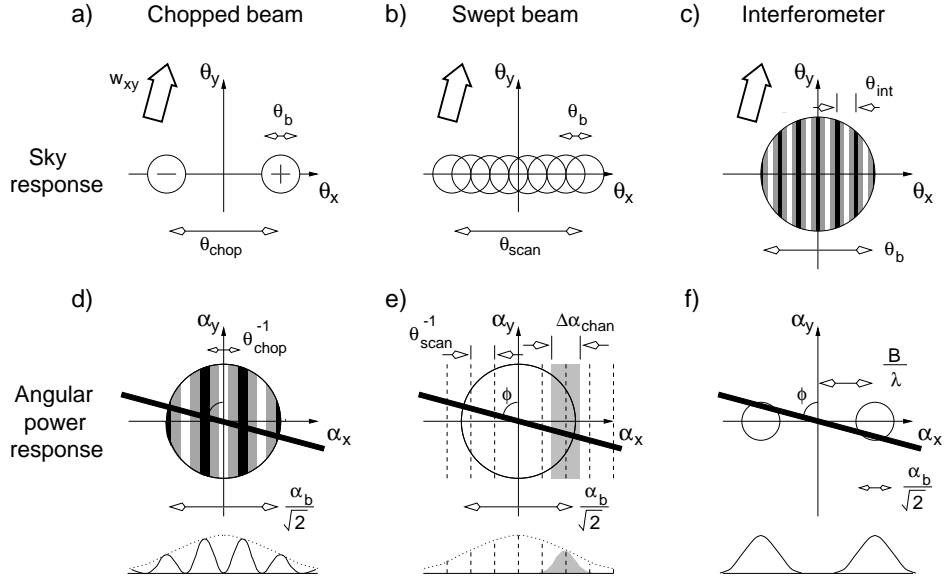


Fig. 3.— Schematic responses of a chopping single aperture (a), a swept beam single aperture (b) and an interferometer (c) to far-field emission on the sky. The square of the Fourier Transform of each sky response is shown in (c), (d) and (e). A profile of the spatial response along the α_x -axis is also shown. The arrow in the upper plots indicates the projected wind vector that gives rise to the temporal filter (thin dark strip) shown in the lower figures. Circles represent the half-maximum contour of distributions that are approximately Gaussian. The shaded region in (e) represents one channel in the power spectrum which will have an effective width $\Delta\alpha_{\text{chan}}$ that is larger than the channel spacing $\theta_{\text{sweep}}^{-1}$ if tapering has been applied to the swept ‘slot’ in (b).

expression for ν given above and $\alpha_x = q_x h_{\text{av}} / \sin \epsilon$, $\alpha_y = q_y h_{\text{av}} / \sin \epsilon$. A zero frequency response is obtained for $w_x \alpha_x + w_y \alpha_y = 0$; signals with $\nu < (2t_{\text{av}})^{-1}$ lie in a strip of width $(w_{xy} t_{\text{av}})^{-1} h_{\text{av}} / \sin \epsilon$, centered on this line, shown schematically by the dark strips perpendicular to the projected wind direction in Fig. 3.

2.4. Residual Fluctuation Power

The atmospheric fluctuation power remaining at the output of the instrument is determined by calculating the overlap integral between the unfiltered atmospheric power (Fig. 2) and the spatial and temporal filtering functions for the instrument as depicted in Fig. 3. This is analogous to the application of a window function for assessing the response of an instrument to the CMB power spectrum. The residual fluctuation power is

$$\Delta T_{\text{atm}}^2 = S \left\{ A (\sin \epsilon)^{-8/3} h_{\text{av}}^{5/3} \right\} \left\{ (w_{xy} t_{\text{av}})^{-1} \frac{h_{\text{av}}}{\sin \epsilon} \right\} \quad (5)$$

$$= S \left(A h_{\text{av}}^{8/3} \right) (\sin \epsilon)^{-11/3} w_{xy}^{-1} t_{\text{av}}^{-1}. \quad (6)$$

The second factor in Eq. 5 gives the intensity of the unfiltered atmospheric fluctuation power (Eq. 2); the third factor is the equivalent width of the temporal response. Note that the projected windspeed w_{xy} also depends implicitly on the elevation ϵ of the observations. The rms fluctuation at the output of the instrument due to atmospheric emission is given by $\sqrt{\Delta T_{\text{atm}}^2}$ and is proportional to $t_{\text{av}}^{-1/2}$. The coefficient S depends on the geometry of the instrument; it is the integral of the product of the atmospheric power law and spatial filter $|\hat{R}|^2$ along the length of the temporal filter function. In the next sections expressions are derived for S that apply for the swept beam and interferometer cases, and the chopped beam case, which turns out to be more complicated, is also examined.

2.4.1. Swept beam

If the atmospheric power P_{atm} does not change significantly in the region of overlap between the spatial filter (a particular channel, e.g. the shaded region in Fig. 3c) and the temporal filter (black strip in Fig. 3c), then

$$S_{\text{sweep}} = \left(\frac{\alpha'_x}{\sin \phi} \right)^{-\frac{11}{3}} \exp \left\{ -8 \ln 2 \left(\frac{\alpha'_x}{\alpha_b \sin \phi} \right)^2 \right\} \frac{\Delta \alpha_{\text{chan}}}{\sin \phi}, \quad (7)$$

where α'_x is the angular wavenumber of the channel and ϕ is the angle that \mathbf{w}_{xy} makes with the θ_x -axis. The first factor is the three-dimensional atmospheric power law, the second is the taper imposed by the beam of the aperture, and the third is the length of the temporal filter strip that overlaps with the channel. This expression applies when $\alpha'_x \gg \Delta \alpha_{\text{chan}}$, i.e. the channel is not too

close to the origin in the (α_x, α_y) plane, and the three-dimensional atmospheric model requires $\alpha'_x / \sin \phi \gg h_{\text{av}} / (2\Delta h)$.

The channels with α'_x close to zero may have a significant response to the strong peak in P_{atm} near $(\alpha_x, \alpha_y) = (0, 0)$. Careful thought must be given to the tapering (or ‘windowing’) function applied over the swept slot on the sky, since this determines the profile of the channel as a function of α_x . Little or no tapering leads to strong sidelobes on the channel response; too much tapering substantially reduces the resolution of the power spectrum. Specific cases can be computed numerically if the altitude h_{av} and thickness Δh of the layer are known.

2.4.2. Interferometer

If the atmospheric power P_{atm} does not change significantly in the region of overlap between the spatial filter (circles in Fig. 3f) and the temporal filter (black strip in Fig. 3f), then

$$S_{\text{int}} = \left(\frac{B}{\lambda} \sin \phi\right)^{-\frac{11}{3}} \exp \left\{ -8 \ln 2 \left(\frac{B \cos \phi}{\lambda \alpha_b}\right)^2 \right\} \frac{\alpha_b \sqrt{\pi}}{\sqrt{2 \ln 2}}. \quad (8)$$

The first factor contains the three-dimensional atmospheric power law (assumes $B/\lambda \gg h_{\text{av}}/(2\Delta h)$), the second accounts for the taper of the primary beam, and the last factor is the equivalent width of the Gaussian spatial filter along the direction of the temporal filter strip for both positive and negative α_x (cf. $\Delta\alpha/\sin \phi$ in Eq. 7). The equation applies when the separation of the apertures is much larger than their diameter ($\alpha_b \ll B/\lambda$) and the wind is blowing close to perpendicular to the baseline ($\phi > 60^\circ$). When the wind is closer to parallel there is very little overlap between the spatial and temporal filters (Fig. 3) and ΔT_{atm}^2 is very small compared to the perpendicular case.

If the edge-to-edge separation ΔD of the apertures is small compared to their diameter d , it is necessary to make a numerical calculation of S_{int} . Two different types of aperture were investigated: (1) a truncated Gaussian distribution of the electric field strength with the edge cut-off at the -10 dB level; (2) a truncated Bessel distribution of the electric field, cut off at the first zero. The first is typical for a dish illuminated by a feedhorn, and the second is obtained at the aperture of a corrugated horn. In each case, \hat{R} was calculated by cross-correlating the E-field distribution of two apertures, and $P_{\text{atm}}|\hat{R}|^2$ was then integrated over the length of the temporal filter.

The results are shown in Figure 4, calculated for when the wind is perpendicular to the baseline (the worst case). It was found that the result was almost independent of the transition from the 3D to the 2D turbulence regime. In addition, to a good approximation, $S_{\text{int}}(d/\lambda)^{8/3}$ is a function of $\Delta D/d$, i.e. for fixed $\Delta D/d$, $S_{\text{int}} \propto (d/\lambda)^{-8/3}$. At large values of $\Delta D/d$, there is a $-11/3$ power-law dependence, as predicted by Eq. 8.

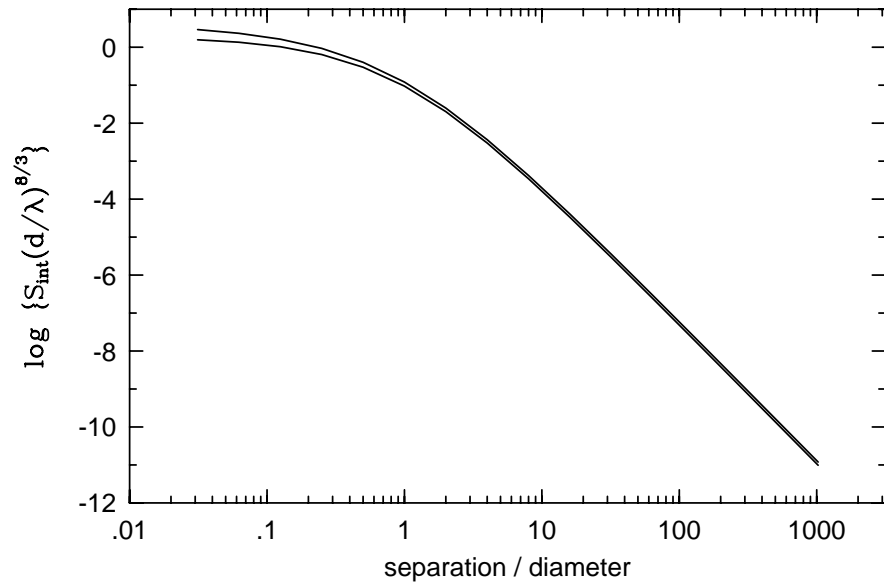


Fig. 4.— Plot of $\log S_{\text{int}}(d/\lambda)^{8/3}$ as a function of the ratio of the edge-to-edge separation to the diameter d of the aperture. The lower of the two lines is for a truncated Gaussian aperture distribution, the upper is for a corrugated horn.

2.4.3. Chopped beam

The two beam chop case shown in Fig. 3d is more complicated because there is significant response to atmospheric power close to the origin, and a substantial variation of P_{atm} in the overlap region of the spatial filter (the \sin^2 fringes in Fig. 3d) and the temporal filter (the black strip in Fig. 3d).

The spatial filter function is given by

$$|\hat{R}|^2 = 4 \sin^2(\pi\theta_c\alpha_x) \quad (9)$$

$$\simeq 4\pi^2\theta_c^2\alpha_x^2 \quad (10)$$

$$\simeq 4\pi^2\theta_c^2(\alpha_w \cos \phi + \alpha_v \sin \phi)^2. \quad (11)$$

The approximation applies close to the origin ($\alpha_x \ll \theta_c^{-1}$) which is the only important source of atmospheric fluctuation power in this case. The value of α_x has been split into components parallel (α_w) and perpendicular to (α_v) the wind direction. With these coordinates, the 3D atmospheric power spectrum is given by $Ah_{\text{av}}^{5/3}(\sin \epsilon)^{-8/3}(\alpha_w^2 + \alpha_v^2)^{-11/6}$ and is valid if the chop angle $\theta_c \ll 2\Delta h \sin \epsilon / h_{\text{av}}$. Then

$$\Delta T_{\text{atm}}^2 = \int_{-C/2}^{+C/2} \int_{-\infty}^{+\infty} Ah^{5/3}(\sin \epsilon)^{-8/3}(\alpha_w^2 + \alpha_v^2)^{-11/6} \quad (12)$$

$$4\pi^2\theta_c^2(\alpha_w \cos \phi + \alpha_v \sin \phi)^2 d\alpha_v d\alpha_w \quad (13)$$

$$= 190Ah_{\text{av}}^2(\sin \epsilon)^{-3}\theta_c^2(1.68 \cos^2 \phi + 2.52 \sin^2 \phi)w_{xy}^{-1/3}t_{\text{av}}^{-1/3} \quad (14)$$

$$\simeq 400Ah_{\text{av}}^2(\sin \epsilon)^{-3}\theta_c^2w_{xy}^{-1/3}t_{\text{av}}^{-1/3}. \quad (15)$$

The integrals have been evaluated analytically, and C is simply the width of the temporal filter ($= (w_{xy}t_{\text{av}})^{-1}h_{\text{av}}/\sin \epsilon$). The expression is applicable when $w_{xy}t_{\text{av}} \gg \theta_ch_{\text{av}}/\sin \epsilon$, i.e., during an integration the fluctuations move a distance somewhat larger than the physical separation of the two beams at the altitude of the fluctuations. It is interesting to note that rms level of the fluctuations goes down as $t_{\text{av}}^{-1/6}$, much more slowly than the usual $t_{\text{av}}^{-1/2}$. This is because the filtered fluctuations are peaked at the center of the temporal filter strip. It is clear that simple chopped observations are very susceptible to atmospheric fluctuations; in practice more complicated three and four beam chops have been used to alleviate this.

2.5. The Unfiltered Fluctuation Strength

The atmospheric brightness fluctuations at a given site and at a given time can be characterized by four parameters: the wind vector \mathbf{w} , the altitude of the turbulent layer h_{av} , the fluctuation intensity A , and the thickness of the layer Δh . Of particular importance is the combination $Ah_{\text{av}}^{8/3}$, which is the measure of fluctuation ‘strength’ relevant to the swept beam and interferometric observations of the microwave background.

In the next sections, data from the South Pole and Chile are analyzed to constrain these parameters. The models developed above are then used to estimate the sky brightness fluctuations that would be expected for an interferometer located at these sites.

3. The South Pole

The South Pole has been chosen as a site for several CMB anisotropy experiments over the past decade (see for example Meinhold & Lubin 1991, Tucker et al. 1993, Dragovan et al. 1994, Platt et al. 1997). It is high (2800 m), extremely cold and dry, and is situated on an expansive ice sheet, with the surface wind dominated by weak katabatic airflow from higher terrain several hundred kilometers away to grid northeast (see discussion in King & Turner 1997). We characterize atmospheric brightness fluctuations at the South Pole using data from the Python telescope, a swept beam CMB experiment, obtained during the austral summer 1996-1997.

3.1. The Python Experiment

The Python telescope, in its configuration for the 1996-1997 season, employs a dual feed 40 GHz HEMT based receiver. The receiver has two corrugated feeds separated by 2.75° on the sky, with separate RF chains, HEMT amplifiers, and backend signal processing. The post-detector output is AC coupled with a cut-off frequency of 1 Hz, and incorporates a low-pass anti-alias filter which attenuates the signal at frequencies above 100 Hz. The RF signal is separated into two frequency bands, centered at 39 GHz and 41.5 GHz with bandwidths of approximately 2 GHz and 5 GHz, respectively. Data from the two bands are combined for atmospheric analysis.

The feeds are in the focal plane of a 0.8 m off-axis paraboloidal mirror, resulting in two 1.1° beams on the sky which are swept through 10° at constant elevation at a rate of 5.1 Hz by a large vertical flat mirror. The two beams are at the same elevation and their sweeps partially overlap on the sky. Beam spillover is reflected to the sky by two sets of shields, one set fixed to the tracking telescope, and a set of larger stationary ground shields which also shield the telescope structure from the sun and any local sources of interference. Data are taken for ~ 30 s while sweeping and tracking a central position on the sky; the telescope is then slewed to another position a few degrees away. Between 5 and 13 pointings are stored in one data file, representing 5 to 10 minutes of observing time. Data were taken over 80% of the period from early December 1996 through early February 1997.

3.2. Data Analysis Technique

In order to differentiate atmospheric fluctuation power from instrument noise, the covariance of the data from the two beams is taken for the portion of each sweep in which their positions overlap on the sky, approximately 6° . Atmospheric brightness fluctuations are correlated between the two beams, while most of the instrument noise is uncorrelated. Thus the signal-to-noise of the correlated fluctuation power can be increased by averaging the covariance over many sweeps on the sky, allowing the atmospheric brightness fluctuation power to be estimated during stable periods when the system is receiver noise limited. The mean covariance represents the mean ‘snapshot’ fluctuation power in the 6° sweep, regardless of the number of sweeps that are subsequently averaged together.

Several instrumental effects are accounted for when estimating the atmospheric brightness fluctuation power:

1. The fluctuation power is corrected for the effect of the anti-alias filter roll-off and backend electronics delay.
2. Correlated 60 Hz line noise is removed from the data.
3. An offset dependent on the position of the sweeping mirror is correlated between the two beams. This is removed by subtracting the component of the signal that is constant on the sky over multiple pointings.

We determine the effect of the 60 Hz line noise filter and stationary signal removal technique on the true atmospheric signal by examining their effect on the data during periods when the data are dominated by atmospheric fluctuations. We calculated that the atmospheric power should be increased by 30% to compensate for the combined effect of these filters and instrumental effects. There is an additional correlated signal due to the stationary ground shield and due to the CMB itself, which is not removed with these techniques. Therefore, the quartiles which we report should be taken as an upper limit of the true atmospheric signal.

3.3. South Pole Atmospheric Fluctuation Data

From the Python data, we determine the South Pole brightness fluctuation power for a 6° sweep at a mean elevation angle of 49° over 2 months of the austral summer (Fig. 5). The atmospheric fluctuations at the South Pole are bimodal in nature, with long periods of high stability broken by periods of high atmospheric fluctuation power. An examination of the meteorological records shows that the latter are always associated with at least partial cloud cover. The infrequent periods of high atmospheric fluctuation power are correlated with a (grid) westerly shift in the wind direction, and are weakly correlated with increased windspeed and precipitable

water vapor content. These correlations indicate that the periods of high atmospheric fluctuation power are associated, at least in part, with synoptically forced moist air from West Antarctica, a condition which occurs infrequently at the pole (Hogan et al. 1982). Variability in the fluctuation power during periods of low atmospheric fluctuation power is consistent with instrument noise.

From these data we construct a cumulative distribution function for the brightness fluctuation power (Fig. 6), and derive quartiles for brightness fluctuation power over the 2 month time period during which the data were taken. The cumulative distribution function for the data files, in which the covariance has been averaged for only a few minutes, is adequate for deriving the 50% and 75% quartiles. However, instrument noise dominates the distribution function at the 25% quartile level; therefore data that are binned in 6 hour intervals are used to derive the 25% quartile. The quartiles for the 2 months of the austral summer 1996-1997 are 0.20 mK², 0.51 mK², and 1.62 mK². To compensate for instrumental filtering effects described above, we increase these values by 30% to 0.27 mK², 0.68 mK², and 2.15 mK². The Python experiment was not operated during the austral winter, so data are not available for this period. However, precipitable water vapor and sky opacity quartiles are lower in the winter months (Chamberlin et al. 1997). It is therefore likely that the atmospheric stability improves during the austral winter as well.

The sharp roll-off of the Python primary beam spatial filter (see Fig. 3e) prevents an accurate determination of the underlying atmospheric angular power spectrum. The angular power spectrum for data that have not been tapered at the edges of the sweep exhibits power proportional to the inverse square of the angular wavenumber. This power law dependence is due to power from low angular wavenumbers (large angular scales) leaking into higher angular wavenumber channels. The observations demonstrate that it is desirable to taper CMB data to reduce contamination from the high atmospheric fluctuation power on large angular scales.

3.4. Estimating the fluctuation intensity

The value of $Ah_{av}^{5/3}$ (Eq. 2) appropriate for the South Pole can be estimated from the rms of the Python measurements. Power spectra for layers of turbulence seen at an elevation of 49° were computed using a full three dimensional integration (similar to Lay 1997). These were then multiplied by the Python spatial filter function $|\hat{R}|^2$ (the sum of all but the DC channel) and integrated to give a value for ΔT_{atm}^2 . The model value for $Ah_{av}^{5/3}$ was then scaled so that the model ΔT_{atm}^2 matched the measured value.

The result is a function of the ratio of the layer thickness to the average altitude of the layer, $\Delta h/h_{av}$. For $\Delta h/h_{av} = 1$, it was found that $Ah_{av}^{5/3} = 0.99\Delta T_{atm}^2$; for $\Delta h/h_{av} = 2$, 0.5 and 0.25, the scale factor changed to 0.89, 1.13 and 1.36, respectively. Therefore the ratio does not have a major effect on the inferred value of $Ah_{av}^{5/3}$. For $\Delta h = h_{av} = 500$ m, the measured quartiles give $Ah_{av}^{5/3} = 0.99\Delta T_{atm}^2 = \{0.27\text{ mK}^2, 0.67\text{ mK}^2, 2.13\text{ mK}^2\}$. Corresponding values for the quantity $Ah_{av}^{8/3}/(\text{mK}^2\text{m})$ (which determines the residual level of fluctuations for swept beam and

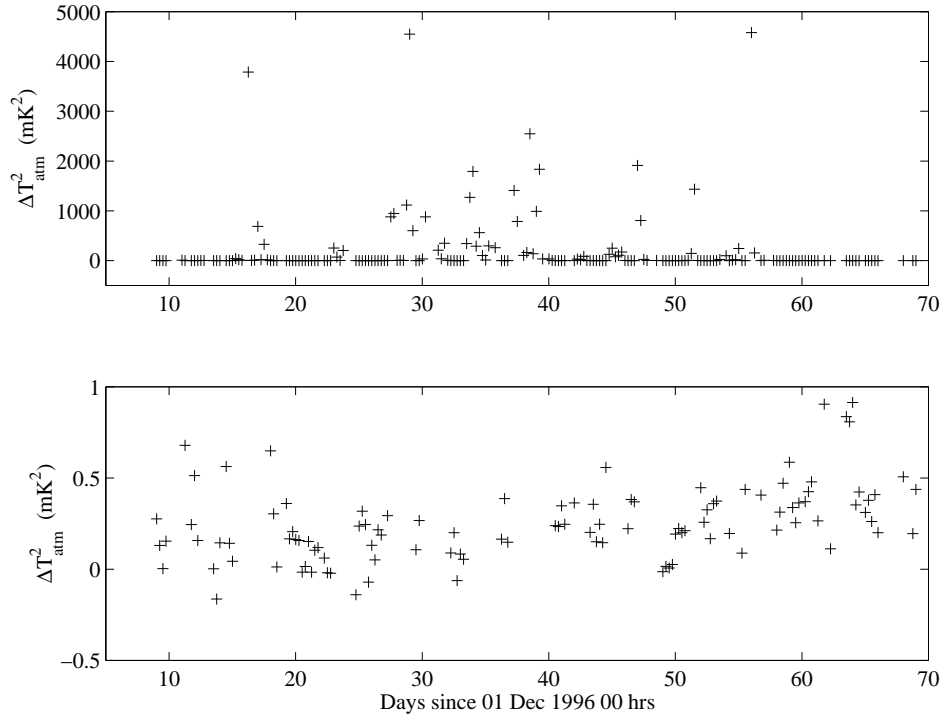


Fig. 5.— The brightness fluctuation power, in mK², for 2 months of Python observations at the South Pole. The measured fluctuation power is for a 6° sweep on the sky, at a mean elevation angle of 49°. The data have been binned in 6 hour intervals to reduce instrument noise. In the lower plot, the scale of the vertical axis is enlarged about zero to show the fluctuation power during stable periods. Even after binning into 6 hour intervals, the variability in the fluctuation power during stable periods is consistent with instrument noise.

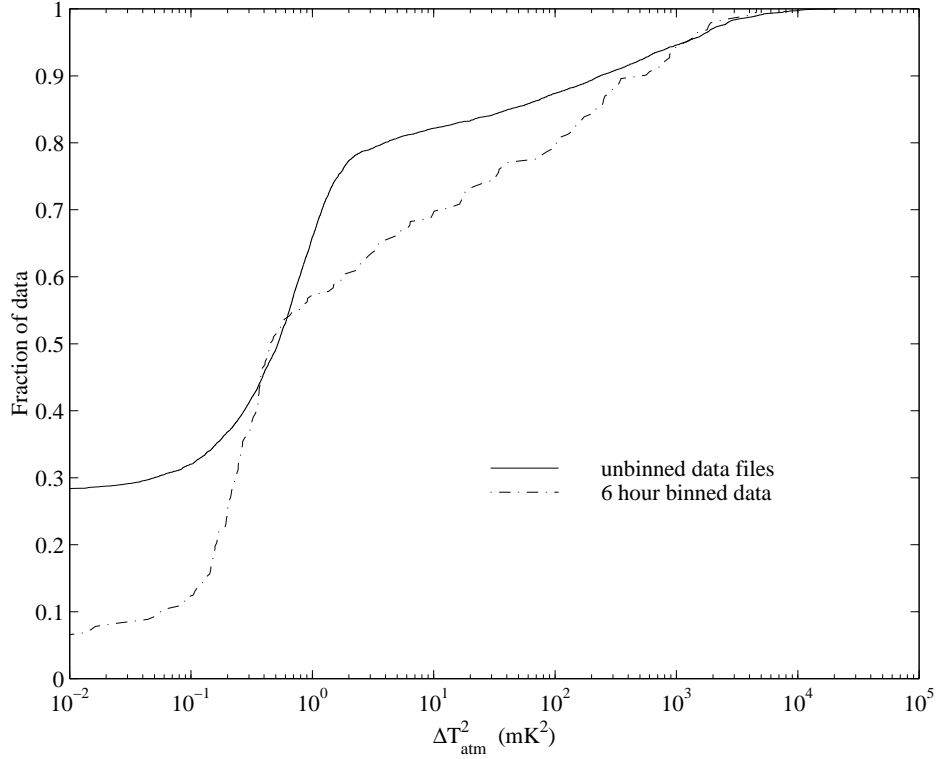


Fig. 6.— The cumulative distribution function of brightness fluctuation power for the Python data shown in Fig. 5. Two distributions are shown, one for unbinned data files taken over a few minutes (solid line), and one for the data binned in 6 hour intervals (dash-dot line). The unbinned data files are adequate to determine the 50% and 75% quartiles, but the 6 hour binned cumulative distribution function is needed to achieve adequate signal-to-noise to estimate the 25% quartile. The increased fraction of high fluctuation power data in the 6 hour binned cumulative distribution function results from binning brief periods of high fluctuation power together with periods of low fluctuation power. The quartiles are 0.20, 0.51 and 1.62 mK^2 (before compensating for instrumental effects).

interferometer experiments – see Eq. 6) are tabulated in Table 1 for three different values of h_{av} . These numbers are appropriate for an observing frequency of 40 GHz. The brightness temperature of fluctuations due to water vapor scales approximately as the square of the observing frequency (except close to the line centers at 22 GHz and 183 GHz), so that $Ah_{\text{av}}^{8/3}$ should be scaled as frequency to the fourth power.

3.5. Altitude of the fluctuations

By combining the data with radiosonde wind measurements, it is possible to determine the altitude of the fluctuations during periods of bad weather. This is illustrated by Fig. 7, which shows the measured emission as a function of angular position θ_x on the sky and time t . The plot represents an interval of 30 s, at a time when the wind was blowing parallel to the sweep direction. The stripes are produced by blobs of water vapor moving from left to right; the diagram shows that a blob moves through an angle of 7° in about 13 s. A 7° angular distance corresponds to a physical length of $0.12h_{\text{av}}/\sin(49^\circ)$, where h_{av} is the average altitude of the fluctuation. The radiosonde launched 2 hours after this dataset indicated a fairly uniform wind speed of $w = 16 \text{ m s}^{-1}$ for the lower 2 km, so a blob is expected to move 208 m in 13 s. Solving for h_{av} gives 1300 m. The slope of the stripes is proportional to h_{av}/w .

In order to average the data together from many 30-s intervals, we compute the power spectrum for each time–angle plot and average those together. The power spectrum for a 30-s interval is calculated by computing the Fast Fourier Transform of the time–angle data from each of the two horns (using a Hann taper to minimize sidelobes), and then calculating the covariance between the two transformed datasets. Figure 7b shows the power spectrum averaged over one hour of data (containing the 30-s interval shown in Fig. 7a). The power is distributed along a radial line, perpendicular to the striping. The gradient of this line is proportional to w/h_{av} ; the overlaid radial lines represent (from vertical) altitudes of 0, 500, 1000, 1500, 2000, 2500 and 3000 m, calibrated using $w = 16 \text{ m s}^{-1}$. The fluctuations have $h_{\text{av}} \sim 1300 \text{ m}$. The physical periodicity is given by w/ν ; e.g. $\nu = 0.1 \text{ Hz}$ corresponds a fluctuation with period 160 m. There is little power present at the origin because the DC level was removed from the time–angle plane before the Hann taper and Fourier transform were applied. The contours appear to fall off faster than would be expected for Kolmogorov turbulence. This is partly due to the effect of the primary beam taper in the angular wavenumber direction, which can be represented by a Gaussian centered on zero with a FWHM size of about 33 rad^{-1} , but may also indicate that these bad weather fluctuations do not follow a Kolmogorov power law.

Average power spectra were computed for all the hours when the wind was parallel to the sweep direction (approximately every 12 hours). Two more examples during periods of bad weather are shown in Fig. 7c and d. The first indicates fluctuations at an altitude of $\sim 500 \text{ m}$; the second shows two components: one at $\sim 300 \text{ m}$ and another at much higher altitude ($> 3 \text{ km}$). Unfortunately it was not possible to detect structure in the power spectrum during stable periods;

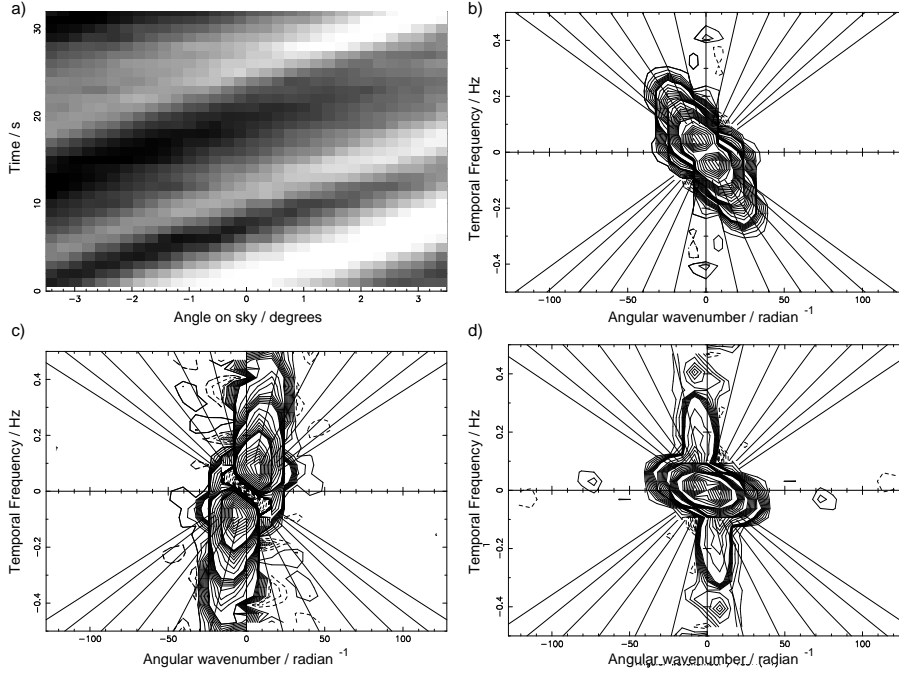


Fig. 7.— a) Time–angle plot for 30 s of Python V data during bad weather, illustrating the striping that results when the wind blows blobs of water vapor along the sweep direction. b) Power spectrum for a 1 hour period which includes the sample shown in (a). Contours are relative to maximum (0.9, 0.8, 0.7, ..., 0.2, 0.1, 0.09, 0.08, etc.). Note that the power is concentrated in a line that is perpendicular to the striping in (a). The radial lines correspond to different altitudes, based on the windspeed measured by radiosonde launches. The y-axis corresponds to ground level, and subsequently shallower lines represent 500, 1000, 1500, 2000, 2500 and 3000 m, respectively. The fluctuations in (a) are at roughly 1500 m above ground. c) Another example showing fluctuations at less than 500 m. d) Two fluctuation components; one very low, the other very high.

the emission is too weak.

In most cases that were measured, the altitude determined for the strong fluctuations, which varies from 300 m to well over 3 km, agreed well with the altitude at which the relative humidity was a maximum (measured by radiosonde launches). This strengthens the case for the connection between clouds and strong fluctuations, and may explain the possible non-Kolmogorov nature of the power spectrum. In the cases of high altitude turbulence ($h_{av} > 3$ km), however, there was no corresponding maximum in the relative humidity and there is generally little water vapor present in the atmosphere. Another mechanism must be at work in these cases.

4. The Atacama Desert in Chile

The Atacama Desert in Northern Chile is extremely dry, and is the proposed location for the next generation of large millimeter-wave arrays, as well as the Cosmic Background Interferometer experiment. The Mobile Anisotropy Telescope has been already been deployed there, and is currently in its second season of observations (L. Page, personal communication). Monitoring of the atmospheric stability at Cerro Chajnantor (the proposed site for the National Radio Astronomy Observatory’s Millimeter Array) has been underway for over 2 years, using a site test interferometer (Radford et al. 1996).

4.1. The site test interferometer

The interferometer used in Chile consists of two dishes 1.8 m in diameter, separated by an East-West baseline of 300 m, that observe the 11 GHz CW beacon from a geostationary communications satellite at an elevation of 36° and an azimuth of 65° . The instrument measures the phase difference between the two received signals, which depends on the difference in the electrical path lengths along the two lines of sight to the satellite. The random component of the fluctuations is dominated by the non-uniform distribution of water vapor in the troposphere being blown over the interferometer, since water vapor has a high refractive index compared to dry air. Quartiles for the rms difference in path length over 1996 are $136 \mu\text{m}$ (25%), $300 \mu\text{m}$ (50%) and $624 \mu\text{m}$ (75%). The data processing is described by Holdaway et al. (1995). These values have not been scaled to zenith.

Water vapor is the principal source of both path length fluctuations and brightness temperature fluctuations. We wish to estimate the latter from a measurement of the former, which requires a conversion factor. This is described in §4.2. It is also necessary to determine A (the intensity of fluctuations integrated through the atmosphere) from the interferometer measurements. This requires a model, and is described in §4.3.

4.2. Converting RMS path to brightness temperature

The millimeter and submillimeter absorption spectrum of water vapor is dominated by a series of rotational line transitions, the lowest of which are at 22 GHz and 183 GHz. At frequencies close to the line centers, the optical depth τ for a given amount of precipitable water vapor (PWV: the depth of liquid water obtained if all the vapor is condensed) is well-determined, but between the lines experiments have shown that the absorption is higher than expected from theory (e.g. Waters 1976, Sutton and Hueckstaedt 1996). The reason for this is still not clear, although several hypotheses have been advanced. At 40 GHz the theoretical absorption from lines is 0.012 per centimeter PWV. The Gaut and Reifenstein (1971) model for the ‘continuum’ absorption increases this to 0.03 cm^{-1} , and is believed to be a reasonable estimate at the frequencies of interest here (Sutton and Hueckstaedt 1996). If the physical temperature of the atmosphere is 250 K, then 1 cm PWV has a brightness temperature of $0.03 \times 250 \text{ K} = 7.5 \text{ K}$. The excess path resulting from 1 cm of water vapor at 250 K is approximately 7 cm (Thompson, Moran and Swenson 1986), so that 1 cm of excess path corresponds to a brightness temperature of 1.1 K, and 1 mK brightness corresponds to $9 \mu\text{m}$ excess path. This conversion should be considered an estimate with an uncertainty of order 50%. A hard upper limit of $22 \mu\text{m mK}^{-1}$ is set by the contribution from line emission only (no continuum term).

Using the value of $9 \mu\text{m mK}^{-1}$, the rms path fluctuation quartiles are mapped to brightness temperature fluctuations of 16, 34 and 69 mK at 40 GHz.

4.3. Estimating A

Since the phase monitor measures the path difference between two lines of sight, its spatial filtering properties are analogous to the chopping instrument depicted in Fig. 3a and d. The main difference is that the lines of sight are parallel to one another through the atmosphere, rather than diverging from the point of observation. As discussed in §2.4, calculation of the residual fluctuation power after spatial and temporal filtering for this configuration requires a model that includes the thickness of the layer containing the fluctuations and the detailed geometry of the observations. The relevant analysis can be found in Lay (1997).

The input model parameters are: baseline 300 m East-West; elevation 36° ; azimuth 65° ; layer thickness 500 m. The windspeed and altitude of the layer are not needed for calculation of A . To obtain rms brightness temperatures of $\{16, 34, 69\}$ mK with the above model parameters requires that $A = \{9.4 \times 10^{-5}, 4.4 \times 10^{-4}, 1.9 \times 10^{-3}\} \text{ mK}^2 \text{ m}^{-5/3}$. The layer thickness has only a small effect on the calculation; if instead the layer is actually 2 km thick, then $A = \{8.0 \times 10^{-5}, 3.7 \times 10^{-4}, 1.6 \times 10^{-3}\} \text{ mK}^2 \text{ m}^{-5/3}$.

The average altitude of the turbulent layer is much more important, but is not known. The quantity $Ah_{\text{av}}^{8/3}/(\text{mK}^2\text{m})$ is tabulated in Table 1 for different values of h_{av} and $\Delta h = 500 \text{ m}$.

This is the value that determines the residual level of fluctuations in a microwave background experiment (Eq. 6).

Quartile	South Pole h_{av}			Chile h_{av}		
	500 m	1000 m	2000 m	500 m	1000 m	2000 m
25%	150	340	800	1500	9400	60,000
50%	370	840	2000	7000	44,000	290,000
75%	1200	2700	6400	29,000	190,000	1,200,000

Table 1: Values of $Ah_{\text{av}}^{8/3}/(\text{mK}^2\text{m})$ (see Eq. 6) for the South Pole as estimated from Python V data (§3), and for the Atacama Desert in Chile estimated from phase monitor data (§4). The Chile numbers have a 50% uncertainty associated with the conversion from refractive index to brightness temperature. Values are appropriate for 40 GHz, but can be scaled to other frequencies based on the emissivity spectrum of water vapor.

5. Example

The analysis and results presented above are applied to calculate the contribution from atmospheric brightness fluctuations to the noise measured by a small interferometer, of the kind that might be used for measurements of the microwave background anisotropy.

We specify a field of view with FWHM of $\theta_b = 3^\circ = 0.053$ rad at a frequency of 40 GHz ($\lambda = 0.75$ cm). The diameter of the aperture required for a Gaussian distribution truncated at the -10 dB level is $d = 1.15\lambda/\theta_b = 16.3$ cm. For a corrugated horn, the diameter is $d = 1.32\lambda/\theta_b = 18.7$ cm, and it is this case that we now investigate further.

The total thermal noise (for the combined sine and cosine components) for a 2-element interferometer with system temperature T_{sys} and bandwidth $\Delta\nu$ is given by

$$\Delta T_{\text{th}} = 0.28 \left(\frac{T_{\text{sys}}}{20 \text{ K}} \right) \left(\frac{\Delta\nu}{5 \text{ GHz}} \right)^{-1/2} \left(\frac{t_{\text{av}}}{\text{s}} \right)^{-1/2} \text{ mK}. \quad (16)$$

The rms atmospheric contribution is given by the square root of Eq. 6:

$$\Delta T_{\text{atm}} = S_{\text{int}}^{1/2} \left(Ah_{\text{av}}^{8/3} \right)^{1/2} (\sin \epsilon)^{-11/6} w_{xy}^{-1/2} t_{\text{av}}^{-1/2}. \quad (17)$$

The value of S_{int} is determined from Figure 4 for a given separation. The value of $Ah_{\text{av}}^{8/3}$ depends on the conditions at the site, as shown in Table 1, as does the projected windspeed w_{xy} .

An ideal site should not significantly compromise the sensitivity of the experiment. We can determine the range of $Ah_{\text{av}}^{8/3}$ for which $\Delta T_{\text{atm}} < \Delta T_{\text{th}}$. From Fig. 4, the maximum value

of $\log S_{\text{int}}(d/\lambda)^{8/3}$ is approximately +0.3, which applies when the wind is perpendicular to the baseline for an interferometer with corrugated horns that very close together. In this example, $d/\lambda = 24.9$, which implies $S_{\text{int}} \leq 3.8 \times 10^{-4}$. Substituting these values into Eq. 17, along with an elevation of 60° and a projected windspeed of 10 m s^{-1} , we obtain

$$\Delta T_{\text{atm}} \leq 8.0 \times 10^{-3} \left(Ah_{\text{av}}^{8/3} \right)^{1/2} t_{\text{av}}^{-1/2} \text{m}^{1/2} \text{s}^{-1/2}. \quad (18)$$

For this to be less than the thermal noise contribution we require $Ah_{\text{av}}^{8/3} < 1.2 \times 10^3 \text{ mk}^2 \text{ m}^{-1}$. Reference to Table 1 indicates that the South Pole should satisfy this requirement most of the time during the summer months, unless the fluctuations are higher than 2 km above the ground. The Chile site appears to be more marginal. It is important to realize that this example was calculated for the extreme case of the wind blowing perpendicular to a baseline for which the apertures are almost touching. The situation is improved by separating the apertures (Fig. 4) and when the wind blows parallel to the baseline (Fig. 3f).

6. Summary

1. The impact of non-uniform emission from the atmosphere on measurements of the cosmic microwave background is analyzed. Chopped beam, swept beam and interferometric measurement schemes are analyzed.
2. The analysis is based on a model where the atmospheric fluctuations are confined to a turbulent layer. Data from phase monitors indicate that there is a transition from a three- to a two-dimensional regime on scales comparable with the thickness of the layer. The outer correlation scale of fluctuations is much larger than the layer thickness. Previous analyses have assumed a much smaller outer scale length and therefore underestimate the level of fluctuations on large scales. The impact of atmospheric fluctuations is assessed by considering the instruments as a combination of spatial and temporal filters that act on the power spectrum of the turbulence.
3. Data from the Python V experiment during summer at the South Pole are analyzed to determine the level of fluctuations. The distribution is bimodal, with stable conditions for 75% of the time and much stronger fluctuations 25% of the time.
4. During normal stable conditions the rms brightness temperature variation in a 6° strip was less than 1 mK. It was not possible to determine either the average altitude or the power spectrum of these very weak fluctuations.
5. The bad weather fluctuations have rms brightness temperature variations of up to 100 mK over a 6° strip of sky, at a frequency of 40 GHz. They are only present when there is at least partial cloud cover. The windspeed as a function of altitude was used to determine the average altitude of the fluctuations. This varied from 500 m to over 4 km, and in most cases

corresponded to the altitude at which the relative humidity was a maximum. The power spectrum measured for these bad weather fluctuations appears to fall off faster than the predicted Kolmogorov power law, although this may be due to the taper imposed by the primary beam. We conclude that these strong fluctuations are probably associated in some way with cloud activity.

6. Path fluctuation data from a satellite phase monitor located in the Atacama Desert in Chile were used to estimate the corresponding level of brightness temperature fluctuations at 40 GHz for that site. Although this conversion is uncertain by a factor of 2, and the result depends strongly on the unknown altitude of the turbulent layer, the two months of South Pole data indicate a significantly lower level of fluctuations compared to the Chile site, as shown in Table 1.
7. The theoretical analysis and experimental measurements were combined to predict the residual atmospheric noise that would be present at the output of a small interferometer of the type that could be used to measure microwave background anisotropy. It was found that the atmospheric contribution is likely to be small compared to the thermal noise when the apertures are well-separated, but that the atmosphere can dominate in cases where the edges of the apertures are separated by only a few wavelengths. For the latter case, a good site is critical.
8. The analysis shows that the average altitude of the turbulent layer has a big impact on the suitability of a site for microwave background measurements. This parameter is not well constrained by the data from either site. Measurement of this altitude should be a priority for future site testing experiments.

Acknowledgments

The authors wish to express their gratitude to all of the members of the Python V observing team: S. R. Platt, M. Dragovan, G. Novak, J. B. Peterson, D. L. Alvarez, J. E. Carlstrom, J. L. Dotson, G. Griffin, W. L. Holzapfel, J. Kovac, K. Miller, M. Newcomb, and T. Renbarger, who provided us with the Python V data. We thank John Kovac, John Carlstrom and Bill Holzapfel for their insights and helpful discussions, and Greg Griffin and Steve Platt for providing assistance with data and code. We thank the South Pole meteorology office for providing weather data. This research was supported in part by the National Science Foundation under a cooperative agreement with the Center for Astrophysical Research in Antarctica (CARA), grant NSF OPP 89-20223. CARA is a National Science Foundation Science and Technology Center.

References

- Andreani, P., Dall’oglio, G., Martinis, L., Piccirillo, L., & Rossi, L. 1990, *Infrared Phys.*, 30, 479
- Armstrong, J. W., & Sramek, R. A., 1982, *Radio Science* 17, 1579
- Chamberlin, R. A., Lane, A. P., & Stark, A. A. 1994, *ApJ*, 476, 428
- Church, S. E. 1995, *MNRAS*, 272, 551
- Coble, K., Dragovan, M., Kovac, J., Halverson, N., Holzappel, W., Knox, L., Dodelson, S., Ganga, K., Alvarez, D., Peterson, J. B., Griffin, G., Newcomb, M., Miller, K., Platt, S. R., & Novak, G. 1998 in preparation
- Coulman, C. E., & Vernin, J., 1991, *Applied Optics* 30, 118
- Davies, R. D., Gutierrez, C. M., Hopkins, J., Melhuish, S. J., Watson, R. A., Hoyland, R. J., Rebolo, R., Lasenby, A. N., & Hancock, S. 1996, *MNRAS*, 278, 883
- Dragovan, M., Ruhl, J., Novak, G., Platt, S., Crone, B., Pernic, R., & Peterson, J. 1994, *ApJ*, 427, L67
- Gaut, N. E., & Reifstein, E. C. III, 1971, *Environmental Res. and Tech. Rep. No. 13* (Lexington, Mass.)
- Hogan, A., Barnard, S., Samson, J., & Winters, W. 1982, *J. Geophys. Res.*, 87, 4287
- Holdaway, M. A., Radford, S. J. E., Owen, F. N., & Foster, S. M. 1995, *Millimeter Array Technical Memo No. 129*
- King, J. C., & Turner, J. 1997, *Antarctic Meteorology and Climatology* (Cambridge: Cambridge University Press), 92
- Kovac, J., Dragovan, M., Schleuning, D. A., Alvarez, D., Peterson, J. B., Miller, K., Platt, S. R., & Novak, G. 1998 in preparation
- Lay, O. P. 1997, *A&AS*, 122, 535
- Leitch, E. M., Readhead, A. C. S., Pearson, T. J., Myers, S. T., & Gulkis, S. 1998, *ApJ*, submitted (astro-ph/9807312)
- Masson, C. R., 1994, *Atmospheric Effects and Calibrations*, In: Ishiguro, M. & Welch, W. J. (eds.) *Astronomy with Millimeter and Submillimeter Wave Interferometry*, ASP Conference Series Vol. 59, p. 87
- Meinhold, P., & Lubin, P. 1991, *ApJ*, 370, L11
- Platt, S. R., Kovac, J., Dragovan, M., Peterson, J. B., & Ruhl, J. E. 1997, *ApJ*, 475, L1
- Radford, S. J. E., Reiland, G., & Shillue, B. 1996, *PASP*, 108, 441

- Ruhl, J. E., Dragovan, M., Platt, S. R., Kovac, J., & Novak, G. 1995, *ApJ*, 453, L1
- Scott, P. F., Saunders, R., Pooley, G., O’Sullivan, C., Lasenby, A. N., Jones, M., Hobson, M. P., Duffett-Smith, P. J., & Baker, J. 1996, *ApJ*, 461, L1
- Sutton, E. C., & Hueckstaedt, R. M. 1996, *A&AS*, 119, 559
- Tatarskii, V. I., 1961, *Wave Propagation in a Turbulent Medium*, Dover: New York
- Tegmark, M., & Efstathiou, G. 1996 *MNRAS*, 281, 1297
- Thompson, A. R., Moran, J. M., & Swenson, G., 1986, *Interferometry and Synthesis in Radio Astronomy*, Wiley–Interscience
- Treuhaft, R. N., Lowe, S. T., Bester, M., Danchi, W. C., & Townes, C. H. 1995, *ApJ* 453, 522
- Tucker, G. S., Griffin, G. S., Nguyen, H. T., & Peterson, J. B. 1993, *ApJ*, 419, L45
- Waters, J. W. 1976, *Methods of Experimental Physics*, Vol. 12B (M. L. Meeks, ed.), pp. 142-176
- Wright, M. C. H. 1996, *PASP*, 108, 520